MOLECULAR MAGNETS

Ultrahard magnetism from mixed-valence dilanthanide complexes with metal-metal bonding

Colin A. Gould[1]†, K. Randall McClain[2]†, Daniel Reta[3]‡, Jon G. C. Kragskow[3], David A. Marchiori[4], Ella Lachman[5,6], Eun-Sang Choi[7], James G. Analytis[5,6], R. David Britt[4], Nicholas F. Chilton[3]*, Benjamin G. Harvey[2]*, Jeffrey R. Long[1,6,8]*

Metal-metal bonding interactions can engender outstanding magnetic properties in bulk materials and molecules, and examples abound for the transition metals. Extending this paradigm to the lanthanides, herein we report mixed-valence dilanthanide complexes $(Cp^{iPr5})_2Ln_2I_3$ (Ln is Gd, Tb, or Dy; Cp^{iPr5}, pentaisopropylcyclopentadienyl), which feature a singly occupied lanthanide-lanthanide σ-bonding orbital of $5d_{z^2}$ parentage, as determined by structural, spectroscopic, and computational analyses. Valence delocalization, wherein the d electron is equally shared by the two lanthanide centers, imparts strong parallel alignment of the σ-bonding and f electrons on both lanthanides according to Hund's rules. The combination of a well-isolated high-spin ground state and large magnetic anisotropy in $(Cp^{iPr5})_2Dy_2I_3$ gives rise to an enormous coercive magnetic field with a lower bound of 14 tesla at temperatures as high as 60 kelvin.

Metal-metal bonding underpins a wide range of phenomena in natural and synthetic systems. For example, in the permanent magnets $Nd_2Fe_{14}B$ and $SmCo_5$, strong interactions between the 5d conduction band and localized lanthanide 4f electrons give rise to a large overall moment that couples with the transition metal 3d band to generate large magnetocrystalline anisotropies at high temperature (*1*). Metal-metal bonding has also been leveraged to make advances in numerous other areas, including multifunctional materials (*2*), catalysis (*3*), molecular electronics (*4*), and molecular magnetism. Of particular relevance here, metal-metal bonding has been used in the design of single-molecule magnets (*5*, *6*), a class of molecules that exhibit intrinsic magnetic bistability and magnetic hysteresis at low temperature (*7*).

Metal-metal bonding necessarily requires diffuse valence orbitals, and thus nearly all molecular examples involve transition metals with diffuse d orbitals (*8*). By contrast, the limited radial extension of the lanthanide valence 4f orbitals has thus far precluded isolation of a coordination compound featuring lanthanide-lanthanide bonding. Notably, in endohedral Ln_2 dimers, the transfer of four or five electrons from the lanthanide (Ln) metals to the fullerene cage has been proposed to result in the formation of a doubly or singly occupied σ-bonding orbital of Ln 6s orbital parentage (*9*). However, Coulombic repulsion between the lanthanide centers is substantially stronger than the bonding interaction, and, as such, these exotic systems are not readily translated to the realm of synthetic molecular chemistry. The isolation of a molecular compound featuring lanthanide-lanthanide bonding would thus represent an important fundamental advance and, furthermore, could enable access to favorable electronic and magnetic properties, given the large magnetic moments and single-ion magnetic anisotropies of the 4f elements. The recent discovery of divalent lanthanide ions with $4f^n5d^1$ electron configurations (*10*) suggested to us that it might be possible to achieve lanthanide-lanthanide bonding in a dilanthanide complex with symmetry-compatible 5d orbitals.

Here, we report the mixed-valence dilanthanide complexes $(Cp^{iPr5})_2Ln_2I_3$ (**1-Ln**; Cp^{iPr5}, pentaisopropylcyclopentadienyl; Ln is Y, Gd, Tb, or Dy), synthesized via reduction of the trivalent precursor complexes $(Cp^{iPr5})_2Ln_2I_4$ with potassium graphite in *n*-hexane (Fig. 1A). The precursor species were prepared by a salt metathesis reaction between anhydrous LnI_3 and $NaCp^{iPr5}$ [supplementary materials (SM) section 1.2], with the sterically hindered Cp^{iPr5} ligand being selected to favor the formation of a dinuclear complex over higher nuclearity clusters (*11*). Structural, spectroscopic, and computational analyses of **1-Ln** reveal that upon reduction, rather than adopting a configuration with discrete $4f^n5d^1$ Ln^{II} and $4f^n$ Ln^{III} ions, the compounds instead exhibit valence delocalization due to the formation of a singly occupied σ-bonding molecular orbital of d_{z^2} parentage. This bonding interaction corresponds to a Robin-Day Class III formalism (*12*), wherein the d electron is equally shared by the two lanthanide centers. Valence delocalization imparts strong parallel alignment of the σ-bonding and f electrons on both lanthanides according to Hund's rules, giving rise to high-spin ground states that are thermally isolated even at room temperature (Fig. 1B) (*13*). In **1-Tb** and **1-Dy**, the combination

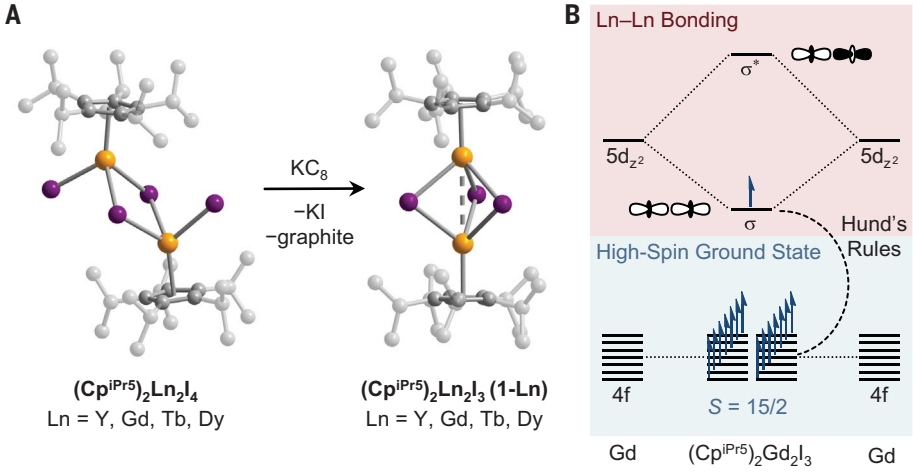

Fig. 1. Synthesis, x-ray diffraction structures, and molecular orbital diagram of dilanthanide complexes. (**A**) Single-electron reduction of $(Cp^{iPr5})_2Ln_2I_4$ (left) with potassium graphite in *n*-hexane affords the compounds $(Cp^{iPr5})_2Ln_2I_3$ (**1-Ln**) (right). The crystal structures shown here correspond to the case where Ln is Gd. Orange, purple, and gray spheres represent Gd, I, and C atoms, respectively; H atoms are omitted for clarity. (**B**) Molecular orbital diagram for $(Cp^{iPr5})_2Ln_2I_3$ illustrates the formation of a singly occupied σ-bonding orbital of $5d_{z^2}$ parentage and alignment of the σ and f electrons on both lanthanides according to Hund's rules. Here, electrons are filled for the case where Ln is Gd.

[1]Department of Chemistry, University of California, Berkeley, Berkeley, CA 94720, USA. [2]US Navy, Naval Air Warfare Center, Weapons Division, Research Department, Chemistry Division, China Lake, CA 93555, USA. [3]Department of Chemistry, School of Natural Sciences, The University of Manchester, Manchester M13 9 PL, UK. [4]Department of Chemistry, University of California, Davis, Davis, CA 95616, USA. [5]Department of Physics, University of California, Berkeley, Berkeley, CA 94720, USA. [6]Materials Sciences Division, Lawrence Berkeley National Laboratory, Berkeley, CA 94720, USA. [7]National High Magnetic Field Laboratory, Florida State University, Tallahassee, FL 32310, USA. [8]Department of Chemical and Biomolecular Engineering, University of California, Berkeley, Berkeley, CA 94720, USA.
***Corresponding author. Email: jrlong@berkeley.edu (J.R.L.); benjamin.g.harvey.civ@us.navy.mil (B.G.H.); nicholas.chilton@manchester.ac.uk (N.F.C.)**
†These authors contributed equally to this work.
‡Present address: Kimika Fakultatea, Euskal Herriko Unibertsitatea (UPV/EHU) and Donostia International Physics Center (DIPC), P. K. 1072, 20080 Donostia, Euskadi, Spain.

of substantial axial magnetic anisotropy and a well-isolated high-spin ground state results in by far the largest coercive magnetic field yet observed for any molecule or molecule-based material.

The solid-state structures of **1-Ln** were determined from single-crystal x-ray diffraction data (Fig. 1A). In all compounds, three iodide anions bridge two metal centers to yield a Ln_2I_3 core with approximate trigonal symmetry, and each metal center is capped with a $(Cp^{iPr5})^-$ ligand. Compounds **1-Y**, **1-Gd**, **1-Tb**, and **1-Dy** display Ln···Ln distances of 3.727(1), 3.769(1), 3.732(1), and 3.713(1) Å (Fig. 2A), respectively, which are within the sum of covalent radii for each metal atom and correspond to formal shortness ratios ranging from 0.961 to 0.981 (*8*, *14*). These ratios are consistent with those determined for homometallic transition metal complexes with half-order metal-metal bonding interactions (*15*–*17*). Notably, the lanthanide ions in **1-Ln** are crystallographically equivalent by a C_2 axis, further suggesting the presence of metal-metal bonding. This observation is supported by complete active space self-consistent field (CASSCF) and density functional theory (DFT) calculations performed on **1-Ln**, which predict the presence of a singly occupied molecular orbital (SOMO) that arises from σ-bonding between the d_{z^2} orbitals of the two lanthanide ions (Fig. 2B; figs. S98, S101, and S104; and table S18). The compounds **1-Ln** possess a similar core structure and symmetry to the well-studied confacial bioctahedral clusters of the type $[M_2X_9]^{n-}$, many of which display metal-metal bonding (*18*, *19*). In these trigonally symmetric clusters, the three μ_2 bridging halide ligands bring the transition metal centers into close proximity, facilitating a σ-bonding interaction between d_{z^2} orbitals.

To corroborate this hypothesis, we synthesized the complex **1-Tm** (SM section 1.2), which is expected to exhibit a $4f^{12}/4f^{13}$ configuration given that Tm^{III} is known to undergo reduction from a $4f^n$ to a $4f^{n+1}$ electron configuration (*10*). Single-crystal x-ray diffraction analysis of **1-Tm** (Fig. 2A) revealed a Tm···Tm distance of 3.960(1) Å, greater than the sum of covalent radii for two Tm atoms [3.80(10) Å] (*14*) as expected for two noninteracting ions. Additionally, the two Tm ions in **1-Tm** show substantial differences in the average Tm–C [2.583(4) versus 2.658(5) Å] and Tm–I [2.954(3) versus 3.212(4) Å] distances, indicative of valence localization. We also prepared the complex salt $[(Cp^{iPr5})_2Dy_2I_3][B(C_6F_5)_4]$ (**2-Dy**) via iodide abstraction from $(Cp^{iPr5})_2Dy_2I_4$ using $[H(SiEt_3)_2][B(C_6F_5)_4]$ (SM section 1.2), which features a Dy_2I_3 core analogous to that in **1-Dy** but with a $4f^9/4f^9$ configuration. Both the Dy···Dy distance and Dy–I–Dy angle in **1-Dy** are smaller than in **2-Dy** [3.713(1) Å and 75.68(1)° versus 3.902(1) Å and 79.65(1)°, respectively; Fig. 2A], despite the larger ionic radius expected for Dy upon reduction. Similar trends have been reported for trihalide-bridged transition metal complexes that display metal-metal bonding (*18*, *19*).

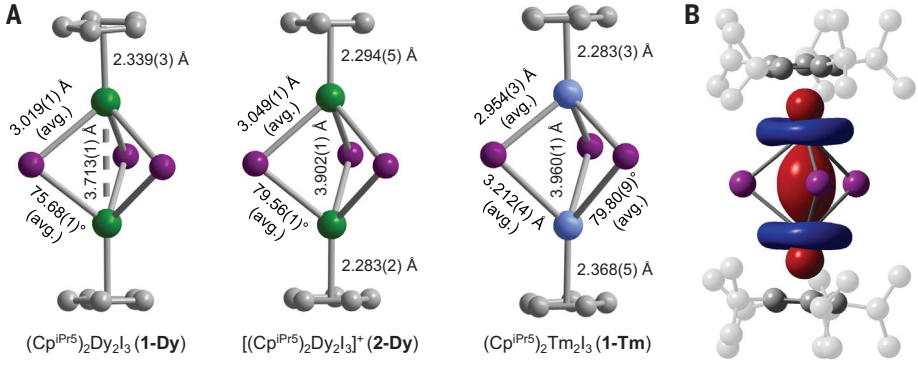

Fig. 2. Structural evidence for lanthanide-lanthanide bonding in $(Cp^{iPr5})_2Ln_2I_3$ (Ln is Y, Gd, Tb, or Dy). (**A**) Comparison of crystal structures of **1-Dy** (left), **2-Dy** (middle), and **1-Tm** (right); green, blue, purple, and gray spheres represent Dy, Tm, I, and C atoms, respectively; isopropyl groups are omitted for clarity. (**B**) SOMO of **1-Gd** as determined by CASSCF calculations; H atoms are omitted for clarity.

Electron paramagnetic resonance (EPR) spectra collected at X-band frequency (9.38 GHz) for **1-Y** (Fig. 3A, fig. S65, and table S8) reveal an axial *g* tensor, consistent with the presence of a σ-bonding SOMO. Here, **1-Y** is used as an $S = ½$ analog for **1-Ln**, because yttrium is a well-established diamagnetic surrogate for late lanthanide ions. Ultraviolet-visible–near-infrared (UV-Vis-NIR) spectra collected for solutions of **1-Y**, **1-Gd**, **1-Tb**, and **1-Dy** in hexanes (Fig. 3B, left) exhibit intense NIR features [molar extinction coefficient (ε) ≥ 5900 M^{-1} cm^{-1}] at the frequency of maximum absorption (ν_{max}) ≈ 15,000 cm^{-1}, which we assign as intervalence charge transfer (IVCT) bands. Similar features are apparent in diffuse reflectance spectra (Fig. 3B, right). By contrast, strong absorption features are absent in the visible and NIR regions of spectra obtained for **1-Tm**, both as a crystalline solid and in hexanes solution (Fig. 3B). CASSCF multiconfigurational pair-density functional theory (*20*) and DFT calculations performed on **1-Y** (SM section 8.3) predict that the IVCT band corresponds to excitation from the symmetric d_{z^2}–d_{z^2} σ-bonding SOMO to the antisymmetric d_{z^2}–d_{z^2} σ-antibonding orbital (fig. S98 and tables S18 and S19), and these calculations enabled identification of additional features in the experimental spectrum due to excitations from σ-bonding to δ- and π-type orbitals (inset of fig. S96). The lowest-energy states that approach localized valence are the δ and δ* states, which are substantially higher in energy than the ground state (8600 to 10,300 cm^{-1} higher in energy, respectively). The full-width-at-half-maximum bandwidths of the IVCT features for **1-Y**, **1-Gd**, **1-Tb**, and **1-Dy** are $\Delta\nu_{1/2}$ = 2370, 2531, 2624, and 2919 cm^{-1}, respectively, considerably narrower than the theoretical bandwidths of $\nu^{o}_{1/2}$ = 5753, 5863, 5916, and 5732 cm^{-1}, respectively (*21*). The parameter $\Gamma = 1 - \Delta\nu_{1/2}/\nu^{o}_{1/2}$ has been proposed for classifying mixed-valence compounds (*22*, *23*), with $\Gamma > 0.5$ associated with Class III systems. For compounds **1-Y**, **1-Gd**, and **1-Tb**, $\Gamma > 0.5$, whereas for **1-Dy**, $\Gamma \approx 0.5$, consistent with valence delocalization. We note that the well-studied Class III mixed-valence complex $[(tmtacn)_2Fe_2(OH)_3]^{2+}$ (tmtacn, 1,4,7-trimethyl-1,4,7-triazacyclononane), which possesses an M_2X_3 core geometry analogous to that in **1-Ln** and a d_{z^2}–d_{z^2} σ-bonding interaction, exhibits an IVCT feature at 13,500 cm^{-1} with $\Gamma \approx 0.5$ (*24*).

Variable-temperature, zero-field cooled dc magnetic susceptibility data obtained for **1-Gd**, **1-Tb**, and **1-Dy** under an applied magnetic field of H_{dc} = 1000 Oe reveal a high-spin ground state in each complex that remains thermally well isolated even up to room temperature (Fig. 4A, open symbols). Indeed, at 300 K, the product of the experimental molar magnetic susceptibility and temperature ($\chi_M T$) for **1-Gd**, **1-Tb**, and **1-Dy** is 30.74, 41.91, and 51.77 electromagnetic units (emu) K mol^{-1}, respectively, substantially greater than the values predicted for noninteracting Ln^{II} and Ln^{III} ions (17.88, 26.24, and 31.18 emu K mol^{-1}, respectively) and instead much closer to the theoretical values of 31.88, 48.74, and 58.68 emu K mol^{-1}, respectively, predicted for parallel alignment of the lanthanide $4f^n$ electrons with the unpaired electron in the σ-bonding orbital. The lower magnitude of the experimental $\chi_M T$ values for **1-Tb** and **1-Dy** relative to the theoretical values is associated with the large magnetic anisotropy, as has been observed previously for strongly coupled lanthanide single-molecule magnets (*25*). A fit to the data for isotropic **1-Gd** (Fig. 4A) using a Heisenberg Hamiltonian for a symmetric exchange-coupled three-spin system (SM section 7.2) gave an exchange constant of J = +387(4) cm^{-1} ($-2J$ formalism, representing spin-spin exchange between the 4f and σ electrons). The exchange constant for **1-Gd** is the largest yet reported

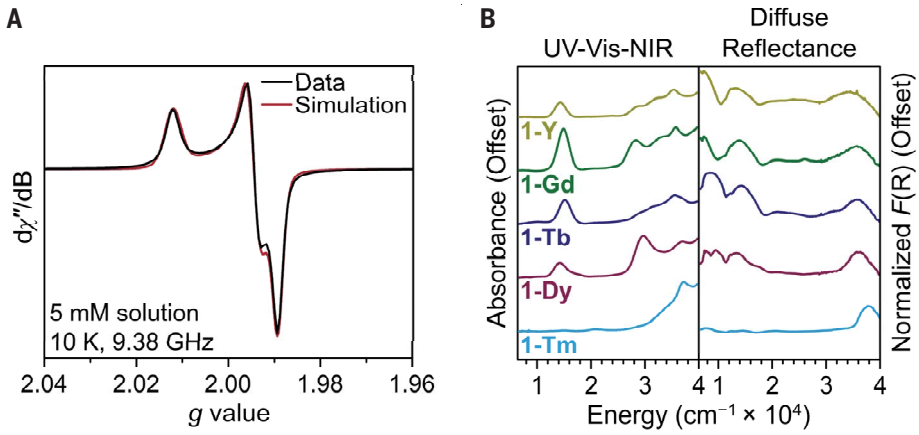

Fig. 3. Characterization of valence delocalization. (**A**) Experimental and simulated EPR data for **1-Y**. (**B**) UV-Vis-NIR and diffuse reflectance spectra for **1-Ln**. The bandwidth of the IVCT transition (ν_{max} ≈ 15,000 cm^{-1}) in **1-Y**, **1-Gd**, **1-Tb**, and **1-Dy** supports valence delocalization. *F*(R) is the Kubelka-Munk transformation of the raw diffuse reflectance spectrum.

for any lanthanide compound, more than twice the value of J = +170(10) cm^{-1} determined for $Gd_2@C_{79}N$ (*9*). Density matrix renormalization group CASSCF calculations (*26*) on **1-Gd** (SM section 8.4) revealed a Heisenberg-like spin ladder (table S20) and a value of J = +389 cm^{-1}, in excellent agreement with the experimental fit value (fig. S100), along with J' = −9 cm^{-1} (4f–4f exchange). Further, broken-symmetry DFT calculations show increasing agreement to experimental values with an increasing fraction of exact exchange (fig. S100 and table S23). Hence, both methods suggest that the exchange coupling is dominated by the direct exchange terms between the σ and 4f electrons (SM section 8.4); thus, the 4f–σ interaction tends to obey Hund's rules.

Field-cooled dc susceptibility data collected for **1-Tb** and **1-Dy** under H_{dc} = 1000 Oe diverge from zero-field cooled data at 70 and 75 K, respectively, indicative of magnetic blocking below these temperatures (Fig. 4A), that is, the pinning of the molecular magnetic moments due to the presence of an energy barrier to relaxation. From dc and ac magnetic relaxation data, we extracted 100-s blocking temperatures of T_b = 65 and 72 K and large thermal barriers to magnetic relaxation of U_{eff} = 1383(45) and 1631(25) cm^{-1} for **1-Tb** and **1-Dy**, respectively (Fig. 4B). Similar data were obtained for dilute solutions of **1-Tb** and **1-Dy**, confirming the molecular origin of the slow magnetic relaxation (tables S13 and S15). The values for **1-Dy** are the highest reported for any single-molecule magnet, surpassing the previous records of T_b = 65 K and U_{eff} = 1541(11) cm^{-1} for $[(Cp^*)Dy(Cp^{iPr5})][B(C_6F_5)_4]$ (Cp*, pentamethylcyclopentadienyl) (*27*).

CASSCF calculations were performed on model systems $[(Cp^{iPr5})_2LnLuI_3]^+$ ($4f^n/4f^{14}$) and $(Cp^{iPr5})_2LnLuI_3$ ($4f^n$–σ–$4f^{14}$) for the cases where Ln is Dy or Tb to elucidate changes to the local magnetic anisotropy due to the presence of the σ-bonding electron and quantify the $4f^n$–σ coupling (SM sections 8.5 and 8.6). The calculated crystal field splitting in $[(Cp^{iPr5})_2DyLuI_3]^+$ is similar to that of the isolated Dy^{III} ions in **2-Dy** (table S33, compare with table S40), whereas the crystal field splitting in $(Cp^{iPr5})_2DyLuI_3$ is substantially enhanced by the σ-bonding electron (table S36); the same is true for $(Cp^{iPr5})_2TbLuI_3$ (table S29, compare with table S26). By generalizing an exchange coupling model proposed for orbitally degenerate ions (SM section 8.5) (*28*), we calculated that the magnetic coupling in $(Cp^{iPr5})_2DyLuI_3$ and $(Cp^{iPr5})_2TbLuI_3$ is dominated by isotropic spin-spin Heisenberg exchange, with J = +524 and +519 cm^{-1}, respectively (−2J formalism). This exchange is stronger than the 4f spin-orbit coupling, and hence the σ electron spin first couples to the total spin of the 4f shell, followed by coupling to the orbital angular momentum. These results are consistent with those for **1-Gd**, revealing that the exchange interactions are dominated by direct exchange, although substantial anisotropy arises in orbitally dependent exchange terms for $(Cp^{iPr5})_2DyLuI_3$ and $(Cp^{iPr5})_2TbLuI_3$ that are absent in **1-Gd**. We next built a model Hamiltonian to describe the full exchange spectrum for **1-Tb** (Fig. 4C); this analysis is more complicated for **1-Dy** owing to the proximity of the first-excited ^6F term to the ground ^6H term of Dy^{III} (SM section 8.6). The ground Kramers doublet for **1-Tb** is M_J = ±25/2, arising from the maximal spin $^{14}I_{25/2}$ term (the ground doublet for **1-Dy** is M_J = ±31/2 from the $^{12}N_{31/2}$ term), although different spin multiplicities are close in energy. Thus, the barrier to magnetic relaxation in **1-Tb** (and, by extension, **1-Dy**) originates from very strong Heisenberg spin-spin coupling between the 4f and σ electrons and large magnetic anisotropy at the lanthanide ion (tables S31 and S39). The larger U_{eff} value for **1-Dy** versus **1-Tb** arises from a combination of a slightly stronger crystal field as well as considerably stronger orbitally dependent exchange interactions (table S35, compare with table S28).

Variable-field magnetization data obtained between ±14 T for **1-Dy** and **1-Tb** revealed wide magnetic hysteresis loops that remain open to 80 and 64 K, respectively, among the highest temperatures reported for any single-molecule magnet (figs. S92 and S94). For both compounds, the coercive field (H_c) increases dramatically as the temperature is lowered, and it was not possible to saturate the magnetization below 68 K for **1-Dy** or 62 K for **1-Tb** using a conventional magnetometer ($H_{dc,max}$ = 14 T). As such, we can only determine a lower bound of H_c ≥ 14 T below 60 K for **1-Dy** (Fig. 4D) and below 50 K for **1-Tb**. This value far surpasses the previous record of 7.9 T at 10 K for the single-molecule magnet $[(Cp^{Me4H}{}_2Tb)_2(\mu\text{–}N_2^{\bullet})]^-$ (*25*) and coercivities of commercial magnets $SmCo_5$ (4.3 T at 4.2 K) (*29*) and $Nd_2Fe_{14}B$ (5.0 T at 80 K) (*30*). Indeed, this lower bound H_c for **1-Dy** and **1-Tb** is the largest yet reported for any molecule or molecule-based material. We can also characterize the magnetic energy density, $(BH)_{max}$, of **1-Dy** and **1-Tb** (SM section 7.7), and these values are more than an order of magnitude greater than those determined for other single-molecule magnets at comparable temperatures and even begin to approach those reported for $SmCo_5$ and $Nd_2Fe_{14}B$ (table S17). Further investigation of the magnetic properties of **1-Tb** and **1-Dy** at higher magnetic fields (H_{dc} > 14 T) is ongoing, and preliminary data indicate that the values of H_c and $(BH)_{max}$ for these compounds are substantially underestimated by measurements between ±14 T. Indeed, field-cooled demagnetization data collected for **1-Tb** between ±35 T reveal a lower-bound estimate for the coercive magnetic field of 25 T at 50 K (fig. S93), and even a field of +35 T is unable to fully saturate the magnetization of **1-Tb** at this temperature.

Notably, **1-Dy** and **1-Tb** display H_c ≥ 14 T at relatively high temperatures, conditions under which the vast majority of single-molecule magnets display closed hysteresis loops. For comparison, only five other molecules—all of the form $[Cp^R{}_2Dy]^+$—show open hysteresis loops at 60 K, and the next highest H_c value at this temperature is 2.1 T for $[(Cp^*)Dy(Cp^{iPr5})]^+$ (*27*). The larger H_c values for **1-Tb** and **1-Dy** relative to $[Cp^R{}_2Dy]^+$ complexes can be attributed to the mitigation of Raman and quantum tunneling processes, which are the predominant pathways for magnetic relaxation in mononuclear single-molecule magnets below the blocking temperature. Indeed, **1-Dy** exhibits a magnetic relaxation time (τ) ~ 1000 s at 67 K, whereas $[(Cp^*)Dy(Cp^{iPr5})]^+$ does not display τ ~ 1000 s until T ≤ 31 K. Previous studies of dinuclear lanthanide compounds have demonstrated that strong magnetic coupling can

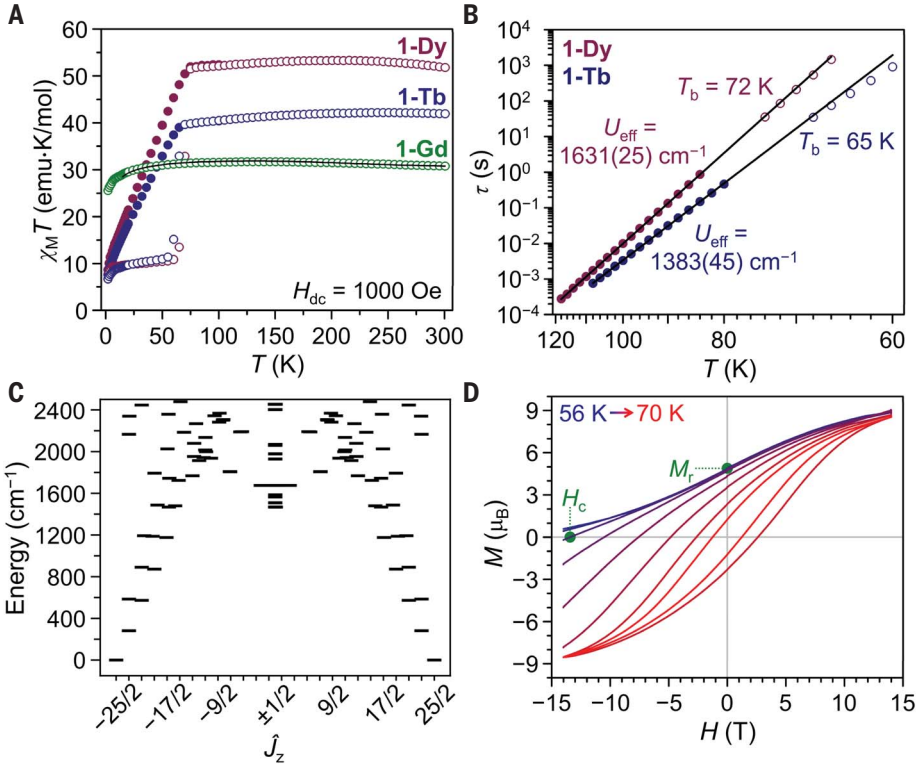

Fig. 4. Magnetic characterization data. (**A**) Field-cooled (filled circles) and zero-field cooled (open circles) dc magnetic susceptibility data for **1-Gd**, **1-Dy**, and **1-Tb**. A fit to the data for **1-Gd** (black line) gives an exchange constant of J = +387(4) cm^{-1}. (**B**) Plots of magnetic relaxation time (τ, log scale) versus T (inverse scale) for **1-Tb** and **1-Dy** derived from ac magnetic susceptibility (filled circles) and dc relaxation (open circles) data; black lines represent fits to the expression $\tau^{-1} = \tau_0^{-1}\exp(-U_{eff}/k_BT)$, yielding U_{eff} and τ_0 values of 1383(45) cm^{-1} and $10^{-11.1(1)}$ s and 1631(25) cm^{-1} and $10^{-12.2(3)}$ s, respectively (k_B, Boltzman constant). (**C**) Ground state splitting in **1-Tb** derived from CASSCF calculations performed on a model $(Cp^{iPr5})_2TbLuI_3$ complex, after downscaling the calculated exchange coupling by 20% (SM section 8.5 and fig. S103). (**D**) Field-cooled demagnetization data from 56 to 66 K (open curves; 2K steps) and magnetic hysteresis data at 68 and 70 K for **1-Dy** (closed loops; sweep rate of 100 Oe s^{-1}).

suppress Raman and quantum tunneling processes, resulting in large values of H_c (*25*). However, the exchange coupling for **1-Dy** and **1-Tb** is an order of magnitude greater than that for other dinuclear lanthanide complexes, and the present compounds are the first examples where the exchange interaction is collinear with the large magnetic anisotropy induced by the crystal field. These two features combine to give the very large values of H_c observed for **1-Dy** and **1-Tb**. Further investigation into the magnetic relaxation dynamics of these compounds is ongoing, and we hope that recent perspectives on the theory of magnetic relaxation (*31*–*33*), new methods for ab initio spin dynamics (*34*, *35*), and more detailed experimental studies (*36*) can be brought to bear to elucidate their behavior.

By exploiting the distinctive electronic structure of divalent lanthanides with $4f^n5d^1$ configurations, we have isolated the complexes $(Cp^{iPr5})_2Ln_2I_3$ (**1-Ln**; Ln is Gd, Tb, or Dy) featuring formal lanthanide-lanthanide bonds. Strong parallel alignment of the $4f^n$ electrons on each lanthanide with a single electron in the σ-bonding orbital of $5d_{z^2}$ parentage gives rise to thermally well-isolated, high-spin ground states according to Hund's rules, and, in the case of **1-Tb** and **1-Dy**, record coercivities at liquid nitrogen temperatures that surpass even commercial magnets. It is exciting to consider the prospect of designing extended solids in which such lanthanide-lanthanide bonded units are coupled through exchange interactions as a means of creating powerful next-generation permanent magnets.

REFERENCES AND NOTES

1. L. Lanotte, F. Lucari, L. Pareti, *Magnetic Properties of Matter* (World Scientific, 1996).
2. C. Pfleiderer *et al.*, *Nature* **412**, 58–61 (2001).
3. I. G. Powers, C. Uyeda, *ACS Catal.* **7**, 936–958 (2017).
4. J. F. Berry, in *Metal–Metal Bonding*, G. Parkin, Ed., vol. 136 of *Structure and Bonding*, D. M. P. Mingos, Ed. (Springer, 2010).
5. R. Hernández Sánchez, T. A. Betley, *J. Am. Chem. Soc.* **137**, 13949–13956 (2015).
6. K. Chakarawet, P. C. Bunting, J. R. Long, *J. Am. Chem. Soc.* **140**, 2058–2061 (2018).
7. D. Gatteschi, R. Sessoli, J. Villain, *Molecular Nanomagnets* (Oxford Univ. Press, 2006).
8. F. A. Cotton, C. A. Murillo, R. A. Walton, *Multiple Bonds Between Metal Atoms* (Springer, 2005).
9. F. Liu *et al.*, *Acc. Chem. Res.* **52**, 2981–2993 (2019).
10. M. E. Fieser *et al.*, *J. Am. Chem. Soc.* **137**, 369–382 (2015).
11. W. J. Evans *et al.*, *J. Coord. Chem.* **59**, 1069–1087 (2006).
12. M. B. Robin, P. Day, in vol. 10 of *Advances in Inorganic Chemistry and Radiochemistry*, H. J. Emeléus, A. G. Sharpe, Eds. (Academic Press, 1968), pp. 247–422.
13. Here, we use the term "high-spin ground state" to indicate that the ground state for **1-Ln** (Ln is Gd, Tb, or Dy) possesses the highest possible value of spin (*S*) owing to strong parallel alignment of both the 4f and σ-bonding electrons. The compounds **1-Tb** and **1-Dy** also possess unquenched orbital angular momentum (*L*), and thus the full electronic states are best described by the total angular momentum (*J*).
14. B. Cordero *et al.*, *Dalton Trans.* **2008**, 2832–2838 (2008).
15. R. J. Eisenhart, L. J. Clouston, C. C. Lu, *Acc. Chem. Res.* **48**, 2885–2894 (2015).
16. C. R. Groom, I. J. Bruno, M. P. Lightfoot, S. C. Ward, *Acta Crystallogr. B Struct. Sci. Cryst. Eng. Mater.* **72**, 171–179 (2016).
17. Reference codes YOLYIH, WECDAJ, EHIMAJ, and VADDEJ01 in (*16*).
18. H.-B. Kraatz, P. M. Boorman, *Coord. Chem. Rev.* **143**, 35–69 (1995).
19. F. A. Cotton, D. A. Ucko, *Inorg. Chim. Acta* **6**, 161–172 (1972).
20. G. Li Manni *et al.*, *J. Chem. Theory Comput.* **10**, 3669–3680 (2014).
21. N. S. Hush, *Prog. Inorg. Chem.* **8**, 391–444 (1967).
22. B. S. Brunschwig, C. Creutz, N. Sutin, *Chem. Soc. Rev.* **31**, 168–184 (2002).
23. D. M. D'Alessandro, F. R. Keene, *Chem. Soc. Rev.* **35**, 424–440 (2006).
24. D. R. Gamelin, E. L. Bominaar, M. L. Kirk, K. Wieghardt, E. I. Solomon, *J. Am. Chem. Soc.* **118**, 8085–8097 (1996).
25. S. Demir, M. I. Gonzalez, L. E. Darago, W. J. Evans, J. R. Long, *Nat. Commun.* **8**, 2144 (2017).
26. S. Keller, M. Dolfi, M. Troyer, M. Reiher, *J. Chem. Phys.* **143**, 244118 (2015).
27. F. S. Guo *et al.*, *Science* **362**, 1400–1403 (2018).
28. N. Iwahara, L. F. Chibotaru, *Phys. Rev. B* **91**, 174438 (2015).
29. R. Kütterer, H.-R. Hilzinger, H. Kronmüller, *J. Magn. Magn. Mater.* **4**, 1–7 (1977).
30. C. Benabderrahmane *et al.*, in *Proceedings of the 11th European Particle Accelerator Conference*, I. Andrian, C. Petit-Jean-Genaz, Eds. (EPAC, 2008), pp.WEPC098.
31. L. T. A. Ho, L. F. Chibotaru, *Phys. Rev. B* **97**, 024427 (2018).
32. L. Gu, R. Wu, *Phys. Rev. Lett.* **125**, 117203 (2020).
33. L. Gu, R. Wu, *Phys. Rev. B* **103**, 014401 (2021).
34. D. Reta, J. G. C. Kragskow, N. F. Chilton, *J. Am. Chem. Soc.* **143**, 5943–5950 (2021).
35. M. Briganti *et al.*, *J. Am. Chem. Soc.* **143**, 13633–13645 (2021).
36. A. Chiesa *et al.*, *Phys. Rev. B* **101**, 174402 (2020).
37. C. A. Gould, J. R. Long, Powder x-ray diffraction data, Dryad (2022); https://doi.org/10.6078/D1RT4W.

ACKNOWLEDGMENTS

We thank A. B. Turkiewicz for experimental assistance and M. E. Ziebel, R. A. Murphy, and L. E. Darago for helpful discussions. We also thank K. R. Meihaus and T. D. Harris for editorial assistance. **Funding:** This work was funded by NSF grants CHE-1800252 and CHE-2102603 (C.A.G. and J.R.L.) and 1905397 (E.L. and J.G.A.); the Naval Air Warfare Center Weapons Division (NAWCWD) NISE-219 program (K.R.M. and B.G.H.); ERC grant 2019-STG-851504 (N.F.C.); and Royal Society fellowship URF191320 (N.F.C.). N.F.C. also thanks the University of Manchester and the Computational Shared Facility at the University of Manchester for support. J.G.A. and E.L. acknowledge support from the Gordon and Betty Moore Foundation's EPiQS Initiative through grant GBMF9067. A portion of this work was performed at the National High Magnetic Field Laboratory, which is supported by NSF cooperative agreement no. DMR-1644779 and the state of Florida.
Author contributions: K.R.M. proposed the molecular design as a high-temperature single-molecule magnet target, synthesized all compounds, and collected single-crystal x-ray diffraction data. C.A.G. refined x-ray diffraction data and performed magnetic characterization. D.A.M. and R.D.B. collected and interpreted EPR data. D.R. performed DFT calculations to estimate magnetic coupling and optical excitations. J.G.C.K. and N.F.C. wrote code to extract coupling and anisotropy parameters from CASSCF calculations. N.F.C. performed CASSCF and density matrix renormalization group

calculations and developed the exchange projection model. E.L. collected variable-field magnetization data between ±14 T and E.-S.C. collected variable-field magnetization data between ±35 T. C.A.G., N.F.C., and J.R.L. wrote the manuscript, and K.R.M., D.R., J.G.C.K., D.A.M., E.L., E.-S.C., J.G.A., R.D.B., and B.G.H. contributed to editing.
Competing interests: The authors declare no competing interests.
Data and materials availability: Single-crystal x-ray diffraction data are deposited in the Cambridge Structural Database (CSD) under the codes 2097927 to 2097937. Powder x-ray diffraction data and simulated spectra are deposited in Dryad (*37*).

SUPPLEMENTARY MATERIALS

science.org/doi/10.1126/science.abl5470
Materials and Methods
Figs. S1 to S106
Tables S1 to S42
References (*38*–*79*)

20 July 2021; accepted 1 December 2021
10.1126/science.abl5470

Science

Ultrahard magnetism from mixed-valence dilanthanide complexes with metal-metal bonding

Colin A. GouldK. Randall McClainDaniel RetaJon G. C. KragskowDavid A. MarchioriElla LachmanEun-Sang ChoiJames G. AnalytisR. David BrittNicholas F. ChiltonBenjamin G. HarveyJeffrey R. Long

Science, 375 (6577), • DOI: 10.1126/science.abl5470

Magnetic effects of lanthanide bonding

Lanthanide coordination compounds have attracted attention for their persistent magnetic properties near liquid nitrogen temperature, well above alternative molecular magnets. Gould *et al*. report that introducing metal-metal bonding can enhance coercivity. Reduction of iodide-bridged terbium or dysprosium dimers resulted in a single electron bond between the metals, which enforced alignment of the other valence electrons. The resultant coercive fields exceeded 14 tesla below 50 and 60 kelvin for the terbium and dysprosium compounds, respectively. —JSY

Science (ISSN) is published by the American Association for the Advancement of Science. 1200 New York Avenue NW, Washington, DC 20005. The title *Science* is a registered trademark of AAAS.